X-ray diffraction evaluation of stress in high pressure deformation experiments

Sébastien Merkel[1]

Department of Earth and Planetary Science, University of California, 307 McCone Hall, Berkeley, CA 94720-4767, USA

E-mail: sebastien.merkel@univ-lille1.fr

Abstract
This paper explores the applicability of x-ray diffraction measurements of stress to high pressure deformation experiments. We model measurements of elastic lattice strains in various geometries for both axial and rotational deformation apparatus. We then show that, for most cases, stresses can be inverted from the diffraction data. A comparison between the results of our models and actual experimental data also indicates that plastic deformation can have an influence that is not addressed properly in the elastic models of lattice strains and should therefore be treated with caution.

1. Introduction

The importance of rheological properties for understanding the dynamics and evolution of the deep Earth is well recognized. However, while considerable progress has been achieved in establishing phase diagrams and physical properties of minerals at high pressure and high temperature, very little is known about the rheological properties of these phases under relevant conditions. To address this issue, deformation experiments at high pressure and high temperature are presently being developed [1–5]. In those experiments, a sample is deformed under high pressure while stress and lattice preferred orientation (LPO) are monitored *in situ* using x-ray diffraction.

While stress evaluation using diffraction has been used for decades in the material science community [6–8], its application in high pressure research is recent and has not been fully explored. In particular, models used for the interpretation of diffraction data in high pressure deformation experiments [9] rely on the assumption that (i) the sample is submitted to a stress that is predominantly axial, (ii) no LPO is present in the sample, (iii) plasticity does not affect the measured lattice spacings. Under those conditions, stress can be evaluated in radial or axial

---

[1] Present address: Laboratoire de Structure et Propriétés de l'Etat Solide (UMR CNRS 8008), Université des Sciences et Technologies de Lille, 59655 Villeneuve d'Ascq, France.
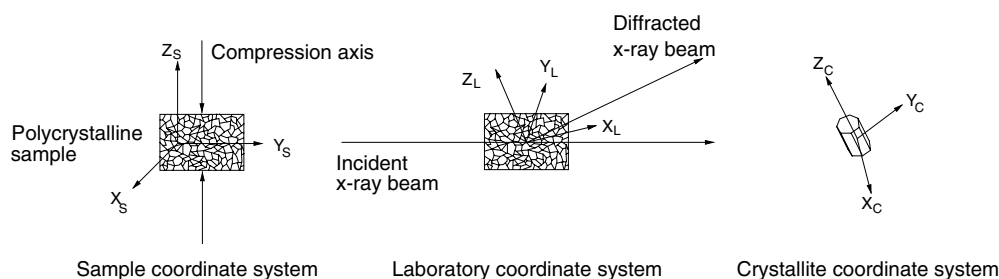
Figure 1. Coordinate systems used in the analysis. The sample coordinate system K_S is defined by the sample environment, with $\mathbf{Z}_S$ parallel to the deformation direction. The laboratory coordinate system K_L is defined with $\mathbf{Z}_L$ parallel to the bisector between the incoming and diffracted beams and $\mathbf{X}_L$ in the plane containing the incoming and diffracted beams, pointing towards the detector. The crystallite coordinate system K_C is defined according to the crystallographic structure. Microscopic physical relations, such as Hooke's law relating the microscopic stresses, strains and single-crystal elastic moduli, should be applied in each crystallite coordinate system K_C. Macroscopic properties such as polycrystalline texture or macroscopic stress are expressed in the sample coordinate system K_S.

diffraction geometry, assuming that the single-crystal elastic moduli of the sample have been estimated independently. However, these assumptions have raised controversies and results obtained using this technique are not always accepted in the community [10].

In this paper, we address this issue by simulating lattice strain measurements in high pressure deformation experiments using more advanced models that do not make the assumption of pure axial stress and include effects of LPO [11]. Comparison between the results of these models and experimental data can be used to assess the state of stress in the experiment. Those models can also be used to test our ability to invert experimental data from experiments in various geometry. Finally, the last section of the paper presents actual experimental data in order to assess the compatibility between the elastic lattice strain models and actual measurements.

2. Elastic theory of diffraction of a polycrystal under stress

Theories relating measured d-spacings using x-ray diffraction, elastic moduli, stress, and lattice preferred orientations (LPO) have been developed independently by several groups [6, 8, 11–19]. Most models used in high pressure research assume axial symmetry of stress and neglect the effects of LPO [13–18]. However, models for more general stress environments and which include the effects of LPO have already been developed and applied to high pressure diffraction data [11, 20–22]. Therefore, we will only summarize the main features of the theory. Details can be found in [11, 21].

First, the resolution of the problem is greatly simplified by introducing several coordinate systems (figure 1): the crystallite coordinate system K_C, the sample coordinate system K_S, and the laboratory coordinate system K_L. The crystallite coordinate system K_C is defined according to the crystallographic structure. Microscopic physical relations, such as Hooke's law relating the microscopic stresses, strains and single-crystal elastic moduli, should be applied in each crystallite coordinate system K_C. The sample coordinate system K_S is defined by the sample environment, with $\mathbf{Z}_S$ parallel to the deformation direction. Finally, the laboratory coordinate system K_L is defined with $\mathbf{Z}_L$ parallel to the bisector between the incoming and diffracted beams and $\mathbf{X}_L$ in the plane containing the incoming and diffracted beams, pointing towards the detector.

Samples submitted to plastic deformation can develop LPO [23]. In a polycrystal, LPO can be represented in terms of an orientation distribution function (ODF) that can be extracted from high pressure diffraction data [1, 4, 24–26]. This is a probability function for finding an orientation and is normalized such that the integral over the whole orientation space is unity. For each orientation g, the ODF $f(g)$ describes the probability density of finding a crystallite that has the orientation g within dg.

Supposing that approximately the same conditions exist for all grains with the same orientation g, with no incompatibilities at grain boundaries or within the grains themselves, and that we consider an ensemble with a sufficiently large number of grains to be represented statistically by an ODF, ODF-weighted averages can be performed to calculate the polycrystal's macroscopic properties from microscopic quantities. For instance, the macroscopic stress $\overline{\sigma}$ and strain $\overline{\epsilon}$ applied to the polycrystal are

$$\overline{\epsilon} = \overline{\epsilon(g)}^a = \int_G \epsilon(g) f(g) \, dg \tag{1}$$

$$\overline{\sigma} = \overline{\sigma(g)}^a = \int_G \sigma(g) f(g) \, dg, \tag{2}$$

where the superscript a denotes an arithmetic mean over all possible orientations. Under the iso-stress Reuss approximation, the elastic properties of the polycrystal can be calculated directly from the average of the elastic compliances using

$$\overline{S}^{\text{Reuss}} = \overline{S(g)}^a \int_G S(g) f(g) \, dg. \tag{3}$$

Details of the calculation of polycrystal average elastic properties, including effects of LPO, for the Voigt and geometric mean have also been derived [11].

In a diffraction experiment, the position of a peak is directly related to the actual d-spacing of the diffracting plane by the relation

$$\lambda = 2 d \sin \theta, \tag{4}$$

where λ is the x-ray wavelength, d is the lattice plane spacing, and θ is the diffraction angle. For a polycrystal, a diffraction peak is the sum of the contribution of all crystallites in the correct reflection position, that is, with the scattering vector $\mathbf{y}$ parallel to the normal to the diffracting plane $\mathbf{h}_i$ (figure 2). Therefore, the measured d-spacing $\overline{d}_m(y)$ is the ODF-weighted arithmetic mean:

$$\overline{d}_m(y) = \frac{1}{4\pi P(\mathbf{y})} \int_{G_y} d(g) f(g) \, dg, \tag{5}$$

where G_y denotes the subset of crystallites in the diffraction condition and $P(y)$ is the normalized number of crystallites in the reflection position.

It is useful to separate the contribution of the hydrostatic pressure, $\overline{\sigma}_P$, and the deviatoric stress $\overline{\sigma}$, using

$$d = d_0(\overline{\sigma}_P) + d_0 \left(\frac{d - d_0}{d_0} \right) (\overline{\sigma}_P, \overline{\sigma}) = d_0 (1 + \epsilon) \tag{6}$$

as the contribution of $\overline{\sigma}_P$ can be estimated easily using a known equation of state and simple crystallographic relations. The measured d-spacings $\overline{d}$ depend on the hydrostatic pressure $\overline{\sigma}_P$, the deviatoric stress $\overline{\sigma}$, the single-crystal elastic moduli S, the ODF f, the plane under consideration $\mathbf{h}_i$, and the direction of observation $\mathbf{y}$. They are related to an 'experimental' strain

$$\overline{\epsilon}(\overline{\sigma}, S, f, \mathbf{h}_i, \mathbf{y}) = \frac{\overline{d}(\overline{\sigma}_P, \overline{\sigma}, S, f, \mathbf{h}_i, \mathbf{y}) - d_0(\overline{\sigma}_P, \mathbf{h}_i)}{d_0(\overline{\sigma}_P, \mathbf{h}_i)}. \tag{7}$$
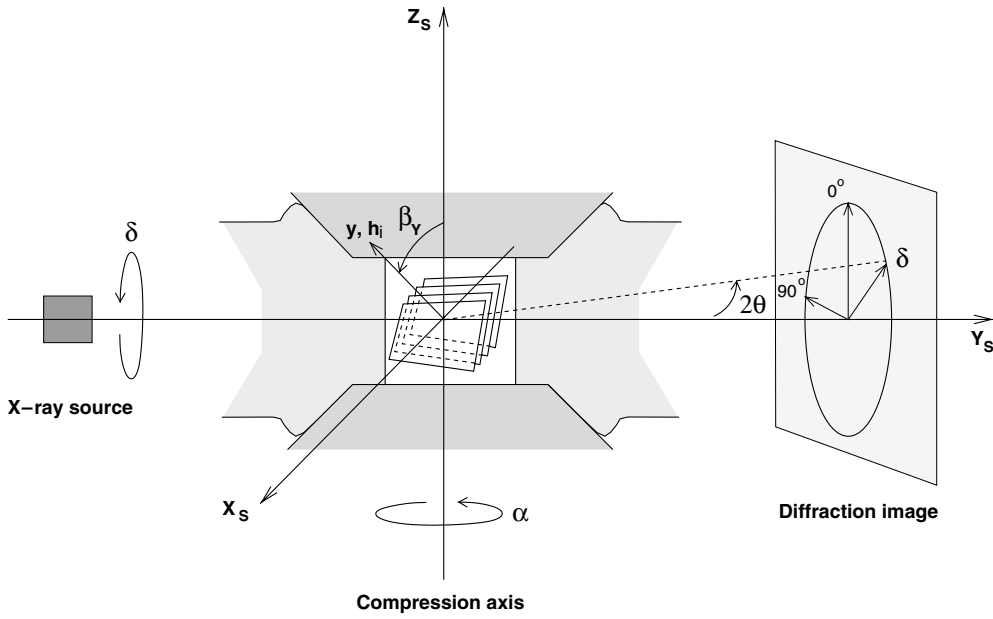
Figure 2. Experimental setup for opposed anvils experiments. The sample is confined between two opposed anvils. In a radial diffraction geometry, a monochromatic x-ray beam is sent with the direction of the incoming beam perpendicular to the anvil axis and the data is collected on an area detector orthogonal to the incoming beam. The position and intensity of the diffraction lines are analysed as a function of the azimuthal angle δ. Directions in the sample coordinate system $K_S(\mathbf{X}_S, \mathbf{Y}_S, \mathbf{Z}_S)$ can be expressed as a function of the two Euler angles α and β, where β and α are related to a rotation around $\mathbf{Y}_S$ and $\mathbf{Z}_S$, respectively. For a given diffraction peak, the normal to the diffracting plane $\mathbf{h}_i$ is aligned with the scattering vector $\mathbf{y}$. Note that the azimuth angle δ is measured in an anti-clockwise direction.

In the laboratory coordinate system K_L (figure 1), the measured strain is equal to the ϵ_{33} component of the strain tensor, and

$$\overline{\epsilon}_{33}^L(\overline{\sigma}, S, f, \mathbf{h}_i, \mathbf{y}) = \frac{1}{4\pi P(\mathbf{y})} \int_{G_\mathbf{y}} \epsilon_{33}^L(\overline{\sigma}, S, \mathbf{h}_i, \mathbf{y}) f(g) \, \mathrm{d}g. \tag{8}$$

Applying Hooke's law to the polycrystal in the laboratory coordinate system, we also have

$$\overline{\epsilon}_{33}^L(\overline{\sigma}, S, f, \mathbf{h}_i, \mathbf{y}) = S_{33kl}^L(S, f, \mathbf{h}_i, \mathbf{y}) \, \overline{\sigma}_{kl}^L, \tag{9}$$

where the laboratory elastic compliances S_{33kl}^L are arithmetic means that only consider the subset of grains that actually contribute to the diffraction.

Finally, the transformation of the stress tensor $\overline{\sigma}_{kl}^L$ to the sample coordinate system, with the appropriate rotation operator $\overline{\sigma}^L = g^{L \leftarrow S}(\mathbf{y}) \, \overline{\sigma}^S$, provides

$$\overline{\epsilon}_{33}^L(\overline{\sigma}, S, f, \mathbf{h}_i, \mathbf{y}) = S_{33kl}^L(S, f, \mathbf{h}_i, \mathbf{y}) g_{klmn}^{L \leftarrow S}(\mathbf{y}) \, \overline{\sigma}_{mn}^S \tag{10}$$

$$= S_{33mn}^{LS}(S, f, \mathbf{h}_i, \mathbf{y}) \overline{\sigma}_{mn}^S, \tag{11}$$

where $\overline{\sigma}_{mn}^S$ is the macroscopic deviatoric stress tensor, expressed in the sample coordinate system K_S.

Calculation of the mixed sample–laboratory coordinate system's macroscopic elastic moduli $S_{33mn}^{LS}(S, f, \mathbf{h}_i, \mathbf{y})$ from the single-crystal elastic moduli S, the ODF f, lattice planes considered $\mathbf{h}_i$ and the direction of orientation $\mathbf{y}$ is not straightforward. In the general case, no analytical relation can be extracted, and all calculations should be performed numerically.

This procedure has been described in detail for the Reuss, Voigt, and geometric (BPGeo) averages [11, 27]. It should be noted that, for the general case of a textured polycrystal, the definition of the Hill average is ambiguous and therefore cannot be used [11]. On the other hand, this procedure does not make any assumption for the geometry of stress and can be applied to the most general cases.

If the assumptions behind the model presented here are verified (approximately the same conditions exist for all grains with the same orientation g, with no incompatibilities at grain boundaries or within the grains themselves, and with an ensemble with a sufficiently large number of grains to be represented statistically by an ODF), and if the single-crystal elastic moduli are known, these equation can be used to simulate the effect of stress on diffraction measurement or to invert residual stresses from diffraction data, including the effects of LPO. If the stress applied to the sample is known, they could also be used to invert effective single-crystal elastic moduli.

3. Models of experimental data

3.1. Main features

In this section, we will model the effect of stress on x-ray diffraction measurements on a polycrystal, with a particular application to the geometries used in high pressure deformation experiments. The results presented here are purely numerical and no attempt will be made to obtain mathematical proofs of inversions capabilities. They should be considered as a catalogue of the effects of stress on measured diffraction patterns with an exploration of our ability to invert stress from experimental data.

For these models, we assume that the sample is a polycrystal of pure hexagonal-close-packed (hcp) Co. In an attempt to improve our understanding of the behaviour of materials under pressure, Co has been studied extensively. Under ambient conditions, it exhibits either the hcp or the metastable face-centred-cubic (fcc) crystal structure and transforms into the fcc structure at 695 K; at high pressure, it transforms into the fcc structure in the range 105–150 GPa [28]. Its elastic properties have been calculated [29], measured using inelastic x-ray scattering (IXS) [30, 31], and deduced from Raman spectroscopy [32] up to high pressure. It has also been studied extensively using radial x-ray diffraction [21, 22]. Therefore, this material is an ideal candidate for testing stress and strain analysis.

In all cases, the sample is assumed to be submitted to an average pressure of 42 GPa. The calculation of unit cell parameters is based on previous measurements of the equation of state [33] and we used the single-crystal elastic moduli and their pressure dependence measured by inelastic x-ray scattering [30]. We also assume that the models developed in section 2 apply, i.e. that the same conditions exist for all grains with the same orientation.

In the forward modelling, the unit cell parameters of the polycrystal are calculated at a pressure 42 GPa using the equation of state. We then calculate the lattice strains resulting from deviatoric stresses using the theory described in section 2 and simulate x-ray diffraction measurements assuming a monochromatic beam of wavelength 0.4 Å. The synthetic data is then processed for stress inversion by fitting deviatoric stress tensor components and d-spacings under equivalent hydrostatic pressure $d_0(\overline{\sigma}_P, hkl)$. Cell parameters a and c are deduced from the fitted $d_0(\overline{\sigma}_P, hkl)$ and later used to invert the hydrostatic pressure.

3.2. Opposed anvil geometry

The developments presented in this section can be applied to various opposed anvil deformation experiments, such as those performed in the D-DIA [3, 5, 10, 34–38], Drickamer

Table 1. Applied stress, inversion parameters, and success in stress inversion for models of the opposed anvils geometry. Stresses are expressed in GPa in the sample coordinate system K_S (figure 2).

Model	Geometry	Applied stress	Inversion model	Success
1	⊥	$\begin{bmatrix} -1.5 & \cdot & \cdot \\ \cdot & -1.5 & \cdot \\ \cdot & \cdot & 3.0 \end{bmatrix}$	$\begin{bmatrix} -t/3 & \sigma_{12} & \sigma_{13} \\ \cdot & -t/3 & \sigma_{23} \\ \cdot & \cdot & 2t/3 \end{bmatrix}$	Yes
2	⊥	$\begin{bmatrix} -2.5 & \cdot & \cdot \\ \cdot & -0.5 & \cdot \\ \cdot & \cdot & 3.0 \end{bmatrix}$	$\begin{bmatrix} \sigma_{11} & \sigma_{12} & \sigma_{13} \\ \cdot & \sigma_{22} & \sigma_{23} \\ \cdot & \cdot & \sigma_{33} \end{bmatrix}$	No
3	⊥	$\begin{bmatrix} -0.5 & \cdot & \cdot \\ \cdot & -2.5 & \cdot \\ \cdot & \cdot & 3.0 \end{bmatrix}$	$\begin{bmatrix} \sigma_{11} & \sigma_{12} & \sigma_{13} \\ \cdot & \sigma_{22} & \sigma_{23} \\ \cdot & \cdot & \sigma_{33} \end{bmatrix}$	No
4	⊥	$\begin{bmatrix} \cdot & 3 & \cdot \\ 3 & \cdot & \cdot \\ \cdot & \cdot & \cdot \end{bmatrix}$	$\begin{bmatrix} -t/3 & \sigma_{12} & \sigma_{13} \\ \cdot & -t/3 & \sigma_{23} \\ \cdot & \cdot & 2t/3 \end{bmatrix}$	Yes
5	⊥	$\begin{bmatrix} \cdot & \cdot & 3 \\ \cdot & \cdot & \cdot \\ 3 & \cdot & \cdot \end{bmatrix}$	$\begin{bmatrix} -t/3 & \sigma_{12} & \sigma_{13} \\ \cdot & -t/3 & \sigma_{23} \\ \cdot & \cdot & 2t/3 \end{bmatrix}$	Yes
6	⊥	$\begin{bmatrix} \cdot & \cdot & \cdot \\ \cdot & \cdot & 3 \\ \cdot & 3 & \cdot \end{bmatrix}$	$\begin{bmatrix} -t/3 & \sigma_{12} & \sigma_{13} \\ \cdot & -t/3 & \sigma_{23} \\ \cdot & \cdot & 2t/3 \end{bmatrix}$	Yes
7	⊥	$g(0, 10°, 30°)\begin{bmatrix} -1.5 & \cdot & \cdot \\ \cdot & -1.5 & \cdot \\ \cdot & \cdot & 3.0 \end{bmatrix}$	$g(0, \beta, \alpha)\begin{bmatrix} -t/3 & \cdot & \cdot \\ \cdot & -t/3 & \cdot \\ \cdot & \cdot & 2t/3 \end{bmatrix}$	Yes

presses [16, 39] or the diamond anvil cell (DAC) [4, 9, 40–47]. Figure 2 presents a typical setup of an experiment in the DAC. In those experiments, a sample is compressed between two anvils and diffraction is performed with the incoming x-ray beam perpendicular to the direction of compression. There are various ways of collecting diffraction patterns, such as using energy-dispersive detectors at several locations [36, 39, 41, 42, 48] or an image area detector [4, 37, 38]. In the present paper, we assume that the measurements are performed on an area detector, but those results can be easily converted to the case of measurement in energy dispersive geometry.

The stress applied to the sample has a strong axial component and most studies conducted in this geometry have assumed that the stress is purely axial, with a cylindrical symmetry around the axis of the anvils. Following those assumptions, models have been developed that relate the measured lattice strains with stress, single-crystal elastic moduli, and lattice preferred orientation [11, 14–18]. However, the validity of the cylindrical symmetry of stress has been questioned. Therefore, in this section, we will model measurements of d-spacings in radial diffraction geometry for various stress configurations. These models are then used to assess our ability to invert stress from the diffraction data.

Stress models that we considered are listed in table 1. Figure 3 presents the simulated lattice strains $\overline{\epsilon}_{33}^{L} = (\overline{d} - d_0)/d_0$ for the 100 line of cobalt as a function of the azimuth angle on the detector δ and $(1 - 3\cos^2 \beta_y)$, where β_y is the angle between the axis of the anvil and the diffracting plane normal. Stress models include (i) models with a pure axial stress and a symmetry axis parallel to the direction of the anvils, (ii) models with triaxial stresses having the principal components of stress aligned with the axis of the sample coordinate system K_S, (iii) models with non-zero shear components of the stress tensor, and (iv) models with a pure axial stress with the symmetry axis tilted from the direction of the anvils [47].

The solid lines in figures 3(a) and (b) indicate the results that we obtain if a pure axial stress is applied to the sample (model 1 in table 1) without effects of LPO (thick solid line)
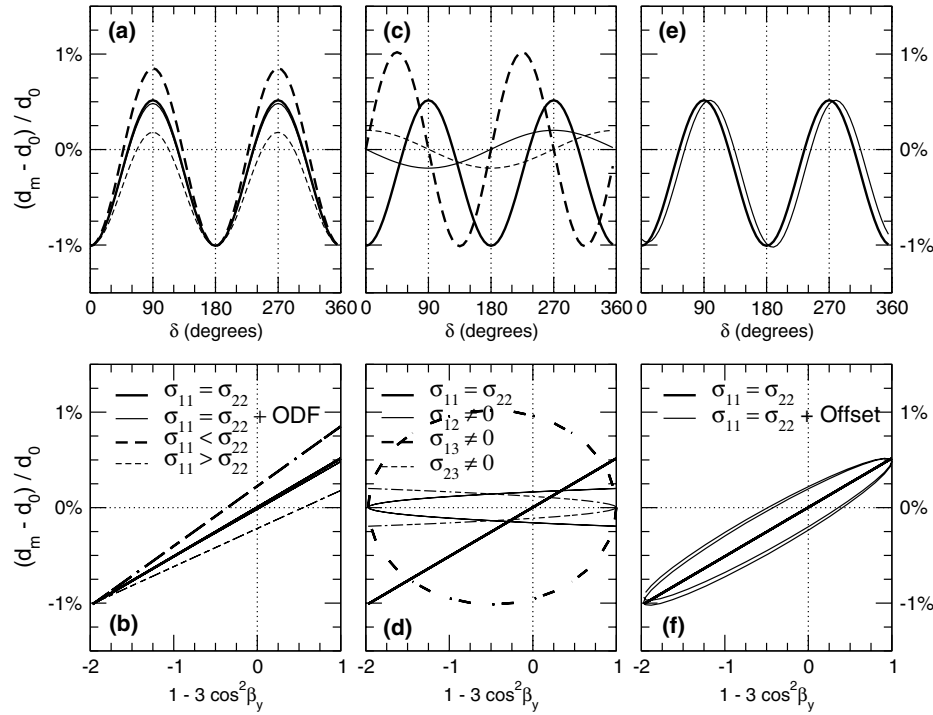
Figure 3. Simulation of measured lattice strains for the 100 line of a cobalt sample in an opposed anvil experiment as a function of the azimuth angle on the detector δ (a), (c), (e) and $(1 - 3\cos^2 \beta_y)$ (b), (d), (f), where β_y is the angle between the anvil axis and the diffracting plane normal, for various stress configurations. Figures (a) and (b) present results for cases where the principal stress directions are aligned with the sample coordinate system (figure 1) with a pure axial stress and no effect of texture (thick solid line), pure axial stress including effects of texture (thin solid line), and triaxial stresses with no effect of texture (dashed lines). Figures (c) and (d) present results for cases with non-zero off-diagonal stress components ($\sigma_{12} \neq 0$, thin solid line; $\sigma_{13} \neq 0$, thick dashed line; $\sigma_{23} \neq 0$, thin dashed line). Figures (e) and (f) present results for a pure axial stress with a maximum stress direction tilted from the anvils direction (thin solid lines). For comparison, the ideal case of pure axial stress with a maximum stress direction aligned with the anvils' direction is indicated in all figures as thick solid lines.

and including effects of LPO (thin solid line) using the ODF measured on a sample of cobalt compressed in a DAC at 42 GPa [22]. The lattice strains vary linearly with $(1 - 3\cos^2 \beta_y)$ for models that do not include effects of LPO [18]; models that include effects of LPO produce slightly curved lines [20]. However, in the present case, the effects of LPO are particularly small and both models can hardly be distinguished. In both cases, stresses can be inverted from the diffraction data.

The dashed lines in figures 3(a) and (b) indicate results for a triaxial stress with the the principal components of stress aligned with the axis of the sample coordinate system K_S and no effects of LPO (models 2 and 3 in table 1). As for the case of pure axial stress, the simulated lattice strains vary linearly with $(1 - 3\cos^2 \beta_y)$. However, stress inversions with σ_{11} and σ_{22} as free parameters will fail consistently. Stress inversion can be performed assuming pure axial stress. For model 2 (thick dashed lines, $\sigma_{11} < \sigma_{22}$), this leads to

$$
\begin{aligned}
&\sigma_P = 39.8 \text{ GPa} \\
&\sigma_{11} = \sigma_{22} = -1.8 \text{ GPa}, \\
&\sigma_{33} = 3.6 \text{ GPa},
\end{aligned}
\tag{12}
$$

that is an under-estimation of pressure and improper stresses. For model 3 (thin dashed lines, $\sigma_{11} > \sigma_{22}$), such an inversion would lead to

$$\sigma_P = 44.1 \text{ GPa}$$
$$\sigma_{11} = \sigma_{22} = -1.2 \text{ GPa}, \qquad\qquad (13)$$
$$\sigma_{33} = 2.4 \text{ GPa},$$

which is an over-estimate of pressure and improper stresses. It should be noted that such a stress configuration can be detected and evaluated by performing additional measurements with the incoming x-ray beam parallel to $\mathbf{X}_S$ or $\mathbf{Z}_S$.

The effects of the shear components of the stress tensor (models 4, 5, and 6 in table 1) are highlighted in figures 3(c) and (d). $\sigma_{12} \neq 0$ and $\sigma_{23} \neq 0$ introduce lattice strains with a period of $360°$ in δ. Maxima and minima of the corresponding lattice strains are located at $\delta = 90°$ and $270°$ for $\sigma_{12} \neq 0$ and $\delta = 0°$ and $180°$ for $\sigma_{23} \neq 0$. On the other hand, $\sigma_{13} \neq 0$ introduces lattice strains with a period of $180°$ in δ with maxima and minima located at $\delta = 45°$, $135°$, $225°$, and $315°$. In all cases, shear components of the stress tensor can be inverted from the diffraction data. Because of the very different nature of the effect of each shear component of the stress tensor on lattice strains, all components can be deduced independently, from a single measurement.

Finally, figures 3(e) and (f) present the results obtained for model 7 in table 1. In this case, the stress is supposed to be mainly axial, but the axis of symmetry of the stress tensor is tilted by $\alpha_\sigma = 30° \; \beta_\sigma = 10°$, where β and α indicate rotations around $\mathbf{Y}_S$ and $\mathbf{Z}_S$, respectively. When plotted as function of δ, the lattice strains resemble that of the pure axial case, with a slight offset of the location of minima and maxima. When plotted as a function of $(1 - 3\cos^2 \beta_y)$, they deviate from the straight line that is expected with pure axial stress and form an ellipse. In any case, such a stress can be inverted from the diffraction data (table 1).

3.3. Rotational anvil geometry

In this section, we investigate the effect of deviatoric stresses on x-ray diffraction patterns in settings corresponding to rotational anvil experiments. These experiments are new and have only recently been applied to high pressure deformation [2, 3, 49–51]. Deformation experiments in this geometry are conducted by twisting a thin sample between the anvils, and stresses are measured *in situ* using x-ray diffraction. However, stress measurement using x-ray diffraction in rotational anvil deformation experiments is still very preliminary and the technique has not yet been standardized. One of the difficulties in stress inversion is the presence of an axial stress component superimposed on the shear stresses imposed by the rotation of the anvils.

Here, we simulate x-ray measurements in three geometries (figure 4): (i) with the incoming x-ray beam parallel to the axis of rotation, sampling a region where the sample is deformed in shear perpendicular to the incoming x-ray beam; (ii) with the incoming x-ray beam perpendicular to the axis of rotation, sampling a region where the sample is deformed in shear perpendicular to the incoming x-ray beam; and (iii) with the incoming x-ray beam perpendicular to the axis of rotation, sampling a region where the sample is deformed in shear parallel to the incoming x-ray beam. In all cases, we assume that the diffraction signal has been filtered and that the diffracting portion of the sample is under uniform stress. Table 2 and figure 5 present the stress models considered and the corresponding lattice strains $\overline{\epsilon}_{33}^L = (\overline{d} - d_0)/d_0$ for the 100 line of cobalt as a function of the azimuth angle on the detector δ, respectively.

The simulated lattice strains for measurements in a perpendicular geometry with the direction of shear perpendicular to the incoming x-ray beam are presented in figure 5(a). In this
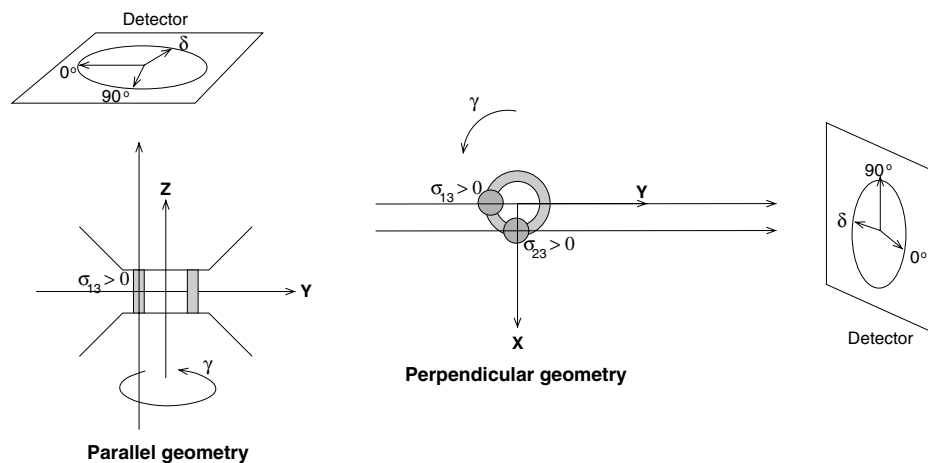
Figure 4. Experimental setup for rotational anvils experiments. The sample is confined between two opposed anvils with a torsion applied to the upper anvil. In the parallel geometry, a monochromatic x-ray beam is sent with the direction of the incoming beam parallel to the anvil axis. In the perpendicular geometry, the x-ray beam is sent with the direction of the incoming beam perpendicular to the anvil axis. The shaded region indicates the region of the sample probed by the synthetic diffraction experiment.
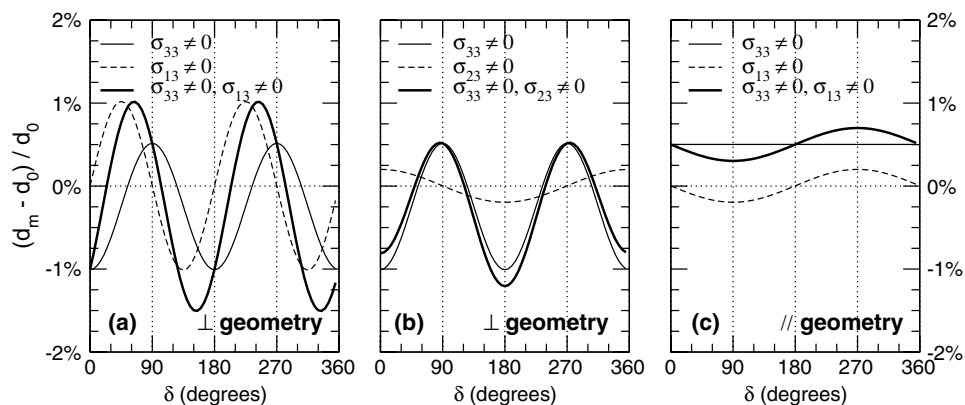

Figure 5. Simulation of measured lattice strains for the 100 line of a cobalt sample in a rotational anvil experiment as a function of the azimuth angle on the detector δ for the geometries described in figure 4: (a) presents the results obtained for an experiment in perpendicular geometry sampling a region where the stress is purely axial (compression, no torsion applied, thin solid line), in simple shear configuration, with the direction of shear perpendicular to the x-ray beam (no compression, torsion applied, thin dashed line), and a combination of the two (compression and torsion applied, thick solid line); (b) presents the results obtained for an experiment in perpendicular geometry sampling a region where the stress is purely axial (compression, no torsion applied, thin solid line), in simple shear configuration, with the direction of shear parallel to the x-ray beam (no compression, torsion applied, thin dashed line), and a combination of the two (compression and tortion applied, thick solid line); and, finally, (c) presents the results obtained for an experiment in parallel geometry sampling a region where the stress is purely axial (compression, no torsion applied, thin solid line), in simple shear configuration (no compression, torsion applied, thin dashed line), and with a combination of the two (compression and torsion applied, thick solid line).

case, the results are very similar to those modelled for the opposed anvil geometry (figure 3). Pure axial stress (thin solid line, model 1), pure shear stress (dashed line, model 2), or a

Table 2. Measurement geometry, applied stress, inversion parameters, and success in stress inversion for models of rotational anvil geometry. Stresses are expressed in GPa in the sample coordinate system K_S (figure 4).

Model	Geometry	Applied stress	Inversion model	Success
1	⊥	$\begin{bmatrix} -1.5 & \cdot & \cdot \\ \cdot & -1.5 & \cdot \\ \cdot & \cdot & 3.0 \end{bmatrix}$	$\begin{bmatrix} -t/3 & \sigma_{12} & \sigma_{13} \\ \cdot & -t/3 & \sigma_{23} \\ \cdot & \cdot & 2t/3 \end{bmatrix}$	Yes
2	⊥	$\begin{bmatrix} \cdot & \cdot & 3 \\ \cdot & \cdot & \cdot \\ 3 & \cdot & \cdot \end{bmatrix}$	$\begin{bmatrix} -t/3 & \sigma_{12} & \sigma_{13} \\ \cdot & -t/3 & \sigma_{23} \\ \cdot & \cdot & 2t/3 \end{bmatrix}$	Yes
3	⊥	$\begin{bmatrix} -1.5 & \cdot & 3 \\ \cdot & -1.5 & \cdot \\ 3 & \cdot & 3 \end{bmatrix}$	$\begin{bmatrix} -t/3 & \sigma_{12} & \sigma_{13} \\ \cdot & -t/3 & \sigma_{23} \\ \cdot & \cdot & 2t/3 \end{bmatrix}$	Yes
4	⊥	$\begin{bmatrix} \cdot & \cdot & \cdot \\ \cdot & \cdot & 3 \\ \cdot & 3 & \cdot \end{bmatrix}$	$\begin{bmatrix} -t/3 & \sigma_{12} & \sigma_{13} \\ \cdot & -t/3 & \sigma_{23} \\ \cdot & \cdot & 2t/3 \end{bmatrix}$	Yes
5	⊥	$\begin{bmatrix} -1.5 & \cdot & \cdot \\ \cdot & -1.5 & 3 \\ \cdot & 3 & 3 \end{bmatrix}$	$\begin{bmatrix} -t/3 & \sigma_{12} & \sigma_{13} \\ \cdot & -t/3 & \sigma_{23} \\ \cdot & \cdot & 2t/3 \end{bmatrix}$	Yes
6	∥	$\begin{bmatrix} -1.5 & \cdot & \cdot \\ \cdot & -1.5 & \cdot \\ \cdot & \cdot & 3 \end{bmatrix}$	$\begin{bmatrix} -t/3 & \sigma_{12} & \sigma_{13} \\ \cdot & -t/3 & \sigma_{23} \\ \cdot & \cdot & 2t/3 \end{bmatrix}$	No
7	∥	$\begin{bmatrix} \cdot & \cdot & 3 \\ \cdot & \cdot & \cdot \\ 3 & \cdot & \cdot \end{bmatrix}$	$\begin{bmatrix} -t/3 & \sigma_{12} & \sigma_{13} \\ \cdot & -t/3 & \sigma_{23} \\ \cdot & \cdot & 2t/3 \end{bmatrix}$	Yes
8	∥	$\begin{bmatrix} -1.5 & \cdot & 3 \\ \cdot & -1.5 & \cdot \\ 3 & \cdot & 3 \end{bmatrix}$	$\begin{bmatrix} -t/3 & \sigma_{12} & \sigma_{13} \\ \cdot & -t/3 & \sigma_{23} \\ \cdot & \cdot & 2t/3 \end{bmatrix}$	No

combination of the two (thick solid line, model 3) have a very different influence on lattice strains, and all can be inverted from the diffraction data.

Simulations of measurements in a perpendicular geometry with the direction of shear parallel to the incoming x-ray beam are presented in figure 5(b). Pure axial stress (thin solid line, model 1) introduces lattice strains with a period of 180° in δ with maxima and minima located at $\delta = 0°$, 90°, 180°, and 270°. Pure shear stress (dashed line, model 4) induces lattice strains with a period of 360° in δ with maxima and minima at $\delta = 0°$ and 180°. A combination of the two stress (thick solid line, model 5) results in the summation of lattice strains induced by the pure axial stress and those induced by the shear component. Both have different periods and can therefore be inverted from the diffraction data.

Finally, figure 5(c) presents the simulated lattice strains for measurements in a parallel geometry. Pure axial stress (thin solid line, model 6) results in a shift in the apparent d-spacing under equivalent hydrostatic pressure d_0. In this case, the axial component of the stress tensor cannot be evaluated from lattice strains only and pressure estimations based on unit cell parameters will be biased. Pure shear stress (dashed line, model 7) results in lattice strains with a period of 360° in δ with maxima and minima at $\delta = 90°$ and 270°. It can be inverted from the data. A combination of axial and pure shear stress (thick solid line, model 8) will result in a shift in the apparent d-spacings under equivalent hydrostatic pressure d_0 and lattice strains with a period of 360° in δ. The shear component of the stress tensor could be inverted from the data, assuming that the shift in apparent d-spacings under equivalent hydrostatic pressure d_0 is properly corrected. This could be done using methods relying on line-width analysis [52, 53], for instance.

4. Example of experimental data

This section will present an example of the applicability of the models described in tables 1 and 2 to actual experimental data. The data presented here have already been published and discussed elsewhere [22]. They were collected at the BL13A beamline of the Photon Factory (Tsukuba, Japan) with a monochromatic x-ray beam of wavelength 0.4258 Å on a 3000×3000 pixel Rigaku image plate with an online reader. Sample-to-detector distance, detector tilt, and pixel size ratios were calibrated using an Ag standard. High pressure and sample deformation was achieved using a DAC equipped with diamonds of 350 μm. To allow diffraction in a direction orthogonal to the compression axis, the sample was confined in an x-ray transparent composite gasket made with amorphous boron, Kapton sheet, and epoxy [54]. The sample was a pure commercial powder of cobalt with a starting grain size of 1–2 μm and a ratio of hexagonal and cubic polymorph of 70%. Pressures were increased up to 42.5 GPa over 24 h.

Figure 6 presents the measured d-spacings as a function of δ and $(1 - 3\cos^2 \beta_y)$ for the 100, 002, and 101 lines of hcp-Co. As observed in previous radial diffraction experiments on Pt [47], a comparison between figures 6 and 3 indicates that the stress is mostly axial, with a slight tilt of the maximum stress direction. An inversion of stress model 7 in table 1 from this data under the Reuss average provides the following parameters:

$$
\begin{aligned}
P &= 42.7 \pm 0.03 \text{ GPa}, \\
t &= 3.2 \pm 0.0 \text{ GPa}, \\
\alpha_\sigma &= 40.1° \pm 1.7°, \\
\beta_\sigma &= -9.5° \pm 0.2°.
\end{aligned}
\tag{14}
$$

However, the recalculated d-spacings do not match the experimental data (thin solid lines in figure 6). Indeed, the amplitude of the lattice strains is under-estimated for lines such as 100 or 002 and over-estimated for 101.

In fact, a polycrystalline sample subjected to plastic deformation can develop heterogeneities from grain to grain, at grain boundaries, or within the grains themselves which can be incompatible with the concept of lattice strain theories. In such cases, the assumption of a single uniform macroscopic stress applied to all grains and lattice planes within the sample can fail, and stresses deduced for various lattice planes might vary [10, 55–59]. In this case, the lattice strain data can be inverted, assuming an (hkl)-dependent uniaxial stress component t_{hkl}. Hence, we adjust the d-spacings under equivalent hydrostatic pressure $d_0(hkl)$ and effective uniaxial stress component t_{hkl} independently for each lattice plane, assuming the offset values of the maximum stress direction α_σ and β_σ found above. Using the elastic moduli measured using inelastic x-ray scattering [30], one finds

$$
\begin{aligned}
P &= 42.7 \pm 0.0 \text{ GPa} \\
t_{100} &= 4.30 \pm 0.03 \text{ GPa} \\
t_{002} &= 3.93 \pm 0.04 \text{ GPa} \\
t_{101} &= 2.53 \pm 0.03 \text{ GPa}
\end{aligned}
\tag{15}
$$

and the recalculated d-spacings are in agreement with the experimental data (thick solid lines in figure 6).

5. Discussion

The results obtained for the models in tables 1 and 2 and figures 3 and 5 demonstrate that lattice strains measured using x-ray diffraction can be a powerful tool for stress evaluation in
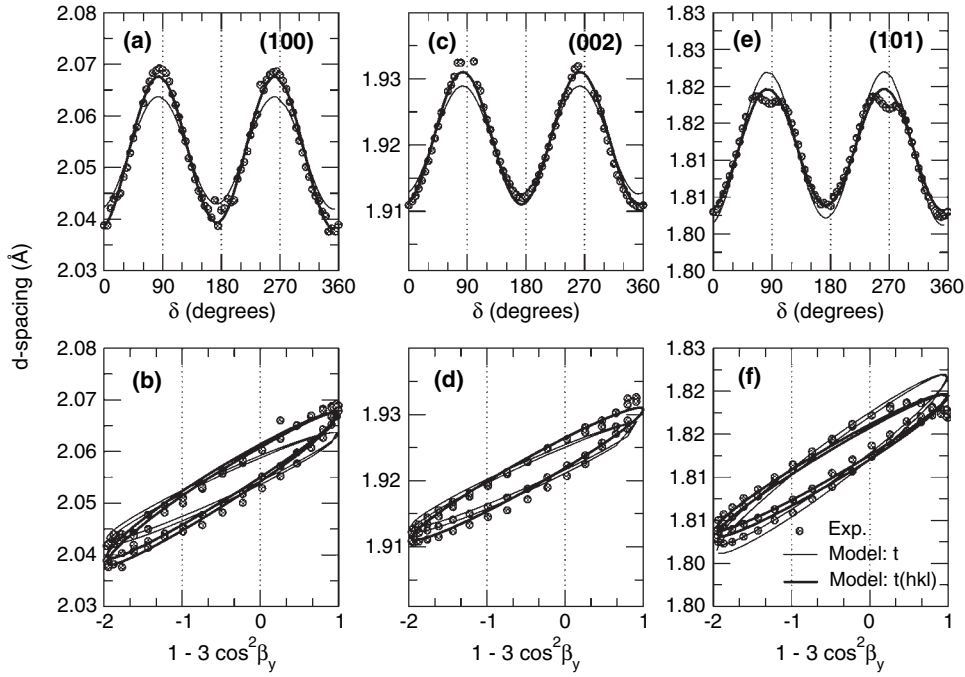
Figure 6. Measured d-spacings in radial diffraction geometry for the 100, 002 and 101 lines of a sample of hcp-Co after plastic deformation in compression in a DAC up to 42 GPa as a function of the azimuth angle on the detector δ (a), (c), (e) and $(1 - 3\cos^2\beta_y)$ (b), (d), (f), where β_y is the angle between the anvil axis and the diffracting plane normal. Symbols are experimental data, thin solid lines are fits to the data assuming a uniform stress for all lattice planes, and thick solid lines are fits to the data assuming (hkl)-dependent stress.

high pressure deformation experiments. Indeed, assuming that no error has been introduced in the measurement itself and that full Debye–Scherrer rings are available, all components of the deviatoric stress tensor can be refined using a single diffraction image, with the exception of σ_{11} and σ_{22}. Moreover, this limitation could be overcome by using complimentary lattice strain analysis on measurements in a different direction or using techniques based on peak profile refinements [52, 53].

Actual experimental data show that the assumption of a single uniform macroscopic stress applied to all grains with the same orientation can fail, and that stresses deduced for various lattice planes can vary [10, 22]. This limitation is known in the material science community, and there are elasto-plastic [55, 59–61], finite-element [57, 62], or continuum mechanics [63] models that can be used to assist data interpretation. Moreover, for most geologically relevant materials such as silicates, the amplitude of the (hkl)-dependence of the measured stresses is smaller than for hcp metals and can simply be included in the errors.

It should be noted, however, that even data that seem to be in agreement with the predictions of the purely elastic models [18] can be affected by plasticity. For instance, the data presented in figure 6 appear to be linear when plotted as a function of $(1 - 3\cos^2\chi)$, where χ is the angle between the maximum stress direction and the diffracting plane normal. The lattice strains $Q(hkl)$ extracted from the data are also consistent with the elastic model [18] when plotted as a function of

$$l_3^2 = 3a^2l^2/[4c^2(h^2 + hk + k^2) + 3a^2l^2]. \tag{16}$$

However, the effective single-crystal elastic moduli extracted from this data are very different from those measured with other techniques [21, 22]. This implies that single-crystal elastic moduli extracted from radial diffraction data should be treated with extreme caution.

Acknowledgments

References

[1] Wenk H R, Matthies S, Hemley R J, Mao H K and Shu J 2000 *Nature* **405** 1044–7
[2] Yamazaki D and Karato S I 2001 *Rev. Sci. Instrum.* **72** 4207–11
[3] Durham W B, Weidner D J, Karato S I and Wang Y 2002 *Plastic Deformation of Minerals and Rocks* (*Reviews in Mineralogy and Geochemistry* vol 51) ed S I Karato and H R Wenk (Washington, DC: Mineralogical Society of America) pp 21–49
[4] Merkel S, Wenk H R, Shu J, Shen G, Gillet P, Mao H K and Hemley R J 2002 *J. Geophys. Res.* **107** 2271
[5] Wang Y, Duhram W B, Getting I C and Weidner D J 2003 *Rev. Sci. Instrum.* **74** 3002–11
[6] Noyan I and Cohen J 1987 *Residual Stress: Measurements by Diffraction and Interpretation* (New York: Springer)
[7] Tanaka K, Kodama S and Goto T (ed) 1993 *X-ray Diffraction Studies on the Deformation and Fracture of Solids* (Amsterdam: Elsevier)
[8] Hauk V 1997 *Structural and Residual Stress Analysis by Nondestructive Methods* (Amsterdam: Elsevier)
[9] Singh A K, Mao H K, Shu J and Hemley R J 1998 *Phys. Rev. Lett.* **80** 2157–60
[10] Weidner D J, Li L, Davis M and Chen J 2004 *Geophys. Res. Lett.* **31** L06621
[11] Matthies S, Priesmeyer H G and Daymond M R 2001 *J. Appl. Crystallogr.* **34** 585–601
[12] Bollenrath F, Hauk V and Müller E H 1967 *Z. Metallk.* **58** 76–82
[13] Singh A K and Kennedy G C 1974 *J. Appl. Phys.* **45** 4686–91
[14] Singh A K 1993 *J. Appl. Phys.* **73** 4278–86
[15] Singh A K and Balasingh C 1994 *J. Appl. Phys.* **75** 4956–62
[16] Funamori N, Yagi T and Uchida T 1994 *J. Appl. Phys.* **75** 4327–31
[17] Uchida T, Funamori N and Yagi T 1996 *J. Appl. Phys.* **80** 739–46
[18] Singh A K, Balasingh C, Mao H K, Hemley R J and Shu J 1998 *J. Appl. Phys.* **83** 7567–75
[19] Howard C J and Kisi E H 1999 *J. Appl. Crystallogr.* **32** 624–33
[20] Matthies S, Merkel S, Wenk H R, Hemley R J and Mao H K 2001 *Earth Planet. Sci. Lett.* **194** 201–12
[21] Merkel S and Yagi T 2006 *J. Phys. Chem. Solids* at press
[22] Merkel S, Miyajima N, Antonangeli D, Fiquet G and Yagi T 2006 *J. Appl. Phys.* at press
[23] Kocks U F, Tomé C and Wenk H R 1998 *Texture and Anisotropy: Preferred Orientations and their Effects on Material Properties* (Cambridge: Cambridge University Press)
[24] Wenk H R, Lonardelli I, Pehl J, Devine J, Prakapenka V, Shen G and Mao H K 2004 *Earth Planet. Sci. Lett.* **226** 507–19
[25] Merkel S, Wenk H R, Gillet P, Mao H K and Hemley R J 2004 *Phys. Earth Planet. Inter.* **145** 239–51
[26] Wenk H R, Ischia G, Nishiyama N, Wang Y and Uchida T 2005 *Phys. Earth Planet. Inter.* **152** 191–9
[27] Matthies S and Humbert M 1995 *J. Appl. Crystallogr.* **28** 254–66
[28] Yoo C S, Cynn H, Söderlind P and Iota V 2000 *Phys. Rev. Lett.* **84** 4132
[29] Steinle-Neumann G, Stixrude L and Cohen R E 1999 *Phys. Rev.* B **60** 791–9
[30] Antonangeli D, Krisch M, Fiquet G, Farber D, Aracne C, Badro J, Occelli F and Requardt H 2004 *Phys. Rev. Lett.* **93** 215505
[31] Antonangeli D, Krisch M, Fiquet G, Badro J, Bossak A, Farber D and Merkel S 2005 *Phys. Rev.* B **72** 134303
[32] Goncharov A F, Crowhurst J and Zaug J M 2004 *Phys. Rev. Lett.* **92** 115502
[33] Fujihisa H and Takemura K 1996 *Phys. Rev.* B **54** 5–7
[34] Li L, Weidner D W, Raterron P, Chen J and Vaughan M 2004 *Phys. Earth Planet. Inter.* **143/144** 357–67
[35] Chen J, Li L, Weidner D J and Vaughan M 2004 *Phys. Earth Planet. Inter.* **143/144** 347–56
[36] Raterron P, Wu Y, Weidner D J and Chen J 2004 *Phys. Earth Planet. Inter.* **145** 149–59
[37] Uchida T, Wang Y, Rivers M L and Sutton S R 2004 *Earth Planet. Sci. Lett.* **226** 117–26
[38] Nishiyama N, Wang Y, Uchida T, Irifune T, Rivers M L and Sutton S R 2005 *Geophys. Res. Lett.* **32** L04307

[39] Uchida T, Funamori N, Ohtani T and Yagi T 1996 *High Pressure Science and Technology* ed W A Trzeciatowski (Singapore: World Scientific) pp 183–5
[40] Kinsland G L and Bassett W A 1977 *J. Appl. Phys.* **48** 978–84
[41] Hemley R J, Mao H K, Shen G, Badro J, Gillet P, Hanfland M and Häusermann D 1997 *Science* **276** 1242–5
[42] Mao H K, Shu J, Shen G, Hemley R J, Li B and Singh A K 1998 *Nature* **396** 741–3
     Mao H K, Shu J, Shen G, Hemley R J, Li B and Singh A K 1999 *Nature* **399** 280 (correction)
[43] Duffy T S, Shen G, Heinz D L, Shu J, Ma Y, Mao H K, Hemley R J and Singh A K 1999 *Phys. Rev.* B **60** 1–10
[44] Kavner A and Duffy T S 2001 *Geophys. Res. Lett.* **28** 2691–4
[45] Shieh S, Duffy T S and Li B 2002 *Phys. Rev. Lett.* **89** 255507
[46] Kavner A 2003 *Earth Planet. Sci. Lett.* **214** 645–54
[47] Kavner A and Duffy T S 2003 *Phys. Rev.* B **68** 144101
[48] Weidner D J, Wang Y and Vaughan M T 1994 *Geophys. Res. Lett.* **21** 753–6
[49] Levitas V I 2004 *Phys. Rev.* B **70** 184118
[50] Xu Y, Nishihara Y and Karato S 2005 *Frontier of High-Pressure Research: Applications to Geophysics* ed J Chen, Y Wang, T S Duffy, G Shen and L F Dobrzhinetskaya (Amsterdam: Elsevier) pp 167–82
[51] Ma Y, Levitas V I and Hashemi J 2005 *SMEC Conf. Abstracts (Miami, FL)*
[52] Singh A K, Liermann H P and Saxena S K 2004 *Solid State Commun.* **132** 795–8
[53] Singh A K, Jain A, Liermann H P and Saxena S K 2006 *J. Phys. Chem. Solids* at press
[54] Merkel S and Yagi T 2005 *Rev. Sci. Instrum.* **76** 046109
[55] Clausen B, Lorentzen T and Leffers T 1998 *Acta Mater.* **46** 3087–98
[56] Daymond M R, Bourke M A M and Von Dreele R B 1999 *J. Appl. Phys.* **85** 739–47
[57] Dawson P, Boyce D, MacEwen S and Rogge R 2001 *Mater. Sci. Eng.* A **313** 123–44
[58] Daymond M R and Bonner N W 2003 *Mater. Sci. Eng.* A **340** 272–80
[59] Li L, Weidner D J, Chen J, Vaughan M T, Davis M and Durham W B 2004 *J. Appl. Phys.* **95** 8357–65
[60] Lodini A 2001 *Radiat. Phys. Chem.* **61** 227–33
[61] Baczmański A, Levy-Tubiana R, Fitzpatrick M E and Lodini A 2004 *Acta Mater.* **52** 1565–77
[62] Dawson P R, Boyce D E and Rogge R B 2005 *Mater. Sci. Eng.* A **399** 13–25
[63] Wang Y D, Wang X L, Stoica A D, Richardson J W and Peng R L 2003 *J. Appl. Crystallogr.* **36** 14–22